Editors' Suggestion

Anomalous Crystal Shapes of Topological Crystalline Insulators

Yutaro Tanaka,[1] Tiantian Zhang,[1,2] Makio Uwaha,[3] and Shuichi Murakami[1,2]
[1]Department of Physics, Tokyo Institute of Technology, 2-12-1 Ookayama, Meguro-ku, Tokyo 152-8551, Japan
[2]TIES, Tokyo Institute of Technology, 2-12-1 Ookayama, Meguro-ku, Tokyo 152-8551, Japan
[3]Science Division, Center for General Education, Aichi Institute of Technology, 1247 Yachigusa, Yakusa-cho, Toyota, Aichi 470-0392, Japan

(Received 12 February 2022; accepted 4 July 2022; published 21 July 2022)

Understanding crystal shapes is a fundamental subject in surface science. It is now well studied how chemical bondings determine crystal shapes via dependence of surface energies on surface orientations. Meanwhile, discoveries of topological materials have led us to a new paradigm in surface science, and one can expect that topological surface states may affect surface energies and crystal facets in an unconventional way. Here, we show that the surface energy of glide-symmetric topological crystalline insulators (TCI) depends on the surface orientation in a singular way via the parity of the Miller index. This singular surface energy of the TCI affects equilibrium crystal shapes, resulting in emergence of unique crystal facets of the TCI. This singular dependence of the topological surface states is unique to the TCI protected by the glide symmetry in contrast to a TCI protected by a mirror symmetry. In addition, we show that such singular surface states of the TCI protected by the glide symmetries can be realized in KHgSb with first-principles calculations. Our results provide a basis for designs and manipulations of crystal facets by using symmetry and topology.

DOI: 10.1103/PhysRevLett.129.046802

Introduction.—One of the fascinating phenomena in crystal physics is characteristic crystal facets. The surface energy and the crystal facets affect morphologies of materials [1–4], and therefore they are vital factors in controlling properties of nanomaterials [5–10]. In particular, the surface energies determine equilibrium crystal shapes [11–13], which can be realized in nanocrystals [14–16], and the surface energies are mainly determined by chemical bondings in crystals [17–20].

We expect that exotic surface states of topological crystalline insulators (TCIs) [21–23] lead to unconventional contributions to surface energies and to unique crystal facets. Although the crystal shapes of TCIs have been observed [24,25], it is not well understood how the topological surface states affect the crystal shapes. Among TCIs with various crystal symmetries [26–35], those with nonsymmorphic symmetries are particularly interesting because of the presence of fractional translations, such as glide mirror and screw rotations [36–44]. Here, we focus on a glide-symmetric TCI with time-reversal ($\mathcal{T}$) symmetry [45–47].

In this Letter, we show that the emergence of the topological surface states depends on the surface orientation in a singular way because of the nonsymmorphic nature of the glide symmetry. In addition, we obtain equilibrium crystal shapes of the TCI from the surface energies. We discover that the crystal shapes of the TCI are affected by the topological surface states, and the TCI has unique facets, unlike the trivial insulator.

Analysis in terms of crystal symmetry.—Here, we consider nonmagnetic TCIs protected by glide symmetry $\hat{G}_y = \{M_y|\frac{1}{2}\hat{\boldsymbol{z}}\}$, i.e., a mirror reflection M_y with respect to the xz plane followed by translation by a half of a lattice vector $\hat{\boldsymbol{z}}$ along the z direction. Henceforth, we take the lattice constants to be unity and let $\hat{\boldsymbol{x}}$, $\hat{\boldsymbol{y}}$, and $\hat{\boldsymbol{z}}$ denote the primitive vectors. Let us first discuss surfaces with a Miller index $(\alpha\beta\gamma)$, which can be written as $\alpha x + \beta y + \gamma z = d$, where d is a constant. Under $\hat{G}_y$, this plane is transformed into $\alpha x - \beta y + \gamma(z - \frac{1}{2}) = d$. The $(\alpha\beta\gamma)$ surface is glide-symmetric, if this plane is identical with a plane $\alpha(x-a) + \beta(y-b) + \gamma(z-c) = d$, where a, b, c are integers. Therefore, when the Miller index satisfies $\beta = 0$ and $\gamma \equiv 0 \pmod 2$, the surface is glide-symmetric. On the other hand, when $\beta = 0$ and $\gamma \equiv 1 \pmod 2$, the surface is not glide-symmetric.

Layer constructions.—To construct a surface theory, we use layer constructions [29,32,42,43], where two-dimensional topological insulator layers are periodically located along the out-of-plane direction. Here, we consider the simplest layer constructions for a glide-symmetric TCI, which consists of two kinds of layers L_A at $z = n$ and L_B at $z = n + \frac{1}{2}$ (n, integer), where L_A and L_B can be interchanged by $\hat{G}_y$. Next, we introduce weak interlayer couplings without closing the gap, while preserving G_y symmetry. Through these procedures, we obtain a three-dimensional (3D) TCI phase protected by G_y symmetry [29,42,48–50].

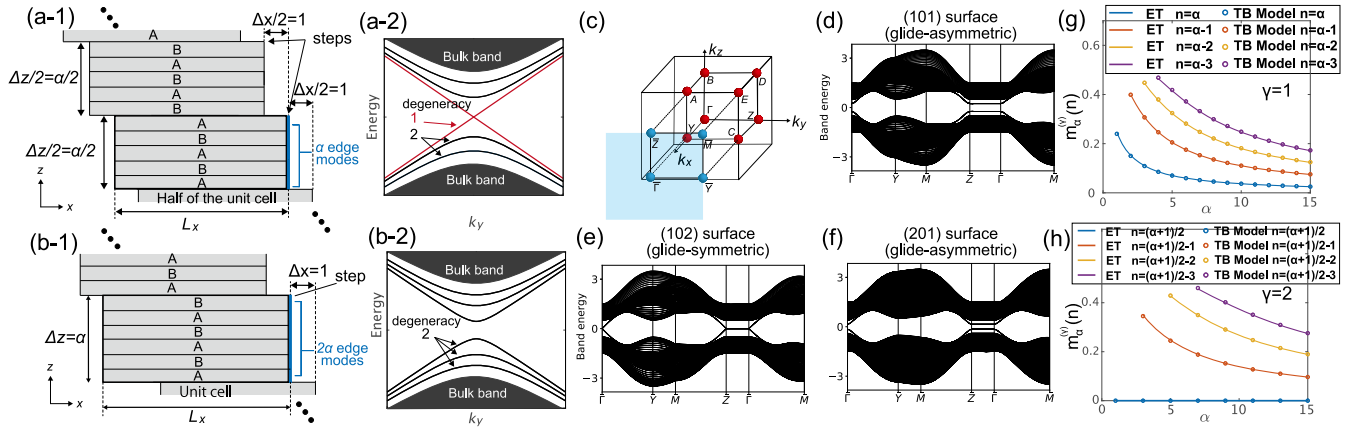

FIG. 1. (a), (b) The steps of the $(\alpha 0 \gamma)$ surface consisting of the layers L_A and L_B with $\gamma = 2$ in (a-1) and $\gamma = 1$ in (b-1), respectively. When $\gamma = 2$, the α edge modes in each step lead to the surface bands in (a-2). When $\gamma = 1$, the 2α edge modes lead to the surface bands in (b-2). (c) The bulk Brillouin zone and the (100) surface Brillouin zone. (d)–(f) The band structures of Eq. (3) with the parameters $t_1 = t_2 = t_3 = m = 1$, $t_{AB} = 0.5$, $t'_{AB} = 0$. (g), (h) Comparison of the surface Dirac masses at $\bar{Z}$ point from the effective theory by Eqs. (1) and (2) (solid lines) with those from the numerical diagonalization of the simple tight-binding model $\mathcal{H}^{(1)}_{\mathrm{TCI}}(\boldsymbol{k})$ (dots), where the parameter is $\delta = 0.247$ in Eqs. (1) and (2).

Henceforth, we consider $(\alpha\beta\gamma)$ surfaces with $\beta = 0$ and $\gamma = 1$, 2 in order to see differences between glide-symmetric $(\gamma = 2)$ and glide-asymmetric $(\gamma = 1)$ cases. Here, the surface becomes equally spaced steps consisting of the layers L_A and L_B [Figs. 1(a-1) and 1(b-1)]. We can classify the configurations of the steps into two types in terms of the number of layers in each step. In the glide-symmetric case with $\gamma = 2$, α is odd because α and γ should be mutually coprime. In such a case, a surface step includes α (= odd) layers. On the other hand, in the glide-asymmetric case with $\gamma = 1$, a single step includes 2α (= even) layers. The odd (even) number of layers in each step leads to gapless (gapped) states.

From our effective surface theory (see Supplemental Material No. 1 and No. 7 [51]), the energy with $\gamma = 2$ is given by $E^{\pm}_n = \pm\sqrt{v^2 k_y^2 + [m^{(\gamma=2)}_\alpha(n)]^2}$, where $m^{(\gamma=2)}_\alpha(n)$ is a Dirac mass

$$m^{(\gamma=2)}_\alpha(n) = 2\delta\cos\left(\frac{\pi n}{\alpha+1}\right) \qquad \left(n = 1, 2, \ldots \frac{\alpha+1}{2}\right), \tag{1}$$

with δ being a real parameter. For the glide-symmetric case with $\gamma = 2$, the bands with $n = 1, 2, \ldots (\alpha-1)/2$ are doubly degenerate, and the band with $n = (\alpha+1)/2$ forms the gapless surface Dirac cone [Fig. 1(a-2)]. On the other hand, in the glide-asymmetric case with $\gamma = 1$, the energy is $E^{\pm}_n = \pm\sqrt{v^2 k_y^2 + [m^{(\gamma=1)}_\alpha(n)]^2}$ [51], where the Dirac mass is

$$m^{(\gamma=1)}_\alpha(n) = 2\delta\cos\left(\frac{\pi n}{2\alpha+1}\right) \qquad (n = 1, 2, \ldots, \alpha). \tag{2}$$

In this case, all the bands are doubly degenerate, and gapless states do not appear [Fig. 1(b-2)].

Next, we calculate surface states of the following simple tight-binding model on a simple orthorhombic lattice:

$$\begin{aligned}\mathcal{H}^{(1)}_{\mathrm{TCI}}(\boldsymbol{k}) = {} & (-m + t_1\cos k_x + t_1\cos k_y)\mu_0\tau_3 \\ & + t_2\sin k_y\mu_3\tau_1\sigma_1 + t_3\sin k_x\mu_0\tau_1\sigma_3 \\ & + (t_{AB} + 2t'_{AB}\cos k_x)\cos\frac{k_z}{2}\mu_1\tau_0, \end{aligned} \tag{3}$$

where σ_i, τ_i, and μ_i $(i = 1, 2, 3)$ are the Pauli matrices, and σ_0, τ_0, and μ_0 are the 2×2 identity matrices. This model is constructed by stacking layers of the two-dimensional topological insulators, as shown in Supplemental Material No. 2 [51], and its topological invariant is given in Supplemental Material No. 3 [51]. Figure 1(c) shows the bulk Brillouin zone and the (100) surface Brillouin zone. In the following, we calculate this model using the PYTHTB package [61], and Figs. 1(d)–1(f) shows the band structures in the slab geometries. For the (101) and (201) surfaces with odd γ [Figs. 1(d) and 1(f)], the surface states are gapped. On the other hand, for the (102) surface with even γ [Fig. 1(e)], the surface states are gapless.

Next, we quantitatively compare the energy gaps of $\mathcal{H}^{(1)}_{\mathrm{TCI}}(\boldsymbol{k})$ with the Dirac mass in Eqs. (1) and (2). Figures 1(g) and 1(h) show a half of the energy gap at $\bar{Z}$ point for various surface bands. This value is to be compared with the Dirac mass in Eqs. (1) and (2). At $\bar{Z}$ point, the ith energy closest to the zero energy is given by $m^{(\gamma=2)}_\alpha(n)$ with $n = (\alpha+1)/2 - (i-1)$ when $\gamma = 2$. When $\gamma = 1$, it is given by $m^{(\gamma=1)}_\alpha(n)$ with $n = \alpha - (i-1)$. The values of the Dirac mass perfectly agree with those from $\mathcal{H}^{(1)}_{\mathrm{TCI}}(\boldsymbol{k})$

[Figs. 1(g) and 1(h)]. The behaviors of the surface states discussed so far for the nonmagnetic TCI also hold true in the magnetic TCI (Supplemental Material No. 4 [51]).

Crystal shape of TCI.—From the surface energies $E_{\mathrm{surf}}^{(\alpha\beta\gamma)}$, we can calculate the equilibrium crystal shape of the TCI by using the Wulff construction [11,51]. The model $\mathcal{H}_{\mathrm{TCI}}^{(1)}(\boldsymbol{k})$ is a minimal model for understanding the behaviors of the topological surface states. On the other hand, the surface energies of this model are quite anisotropic, which leads to the crystal shape with a very small thickness in the z direction (see Supplemental Material No. 3 [51]), and it is difficult to see the effects of the topological surface states on the crystal shape. Thus, we need another model with a more isotropic crystal shape and introduce the following tight-binding model on a simple orthorhombic lattice:

$$\begin{aligned}\mathcal{H}_{\mathrm{TCI}}^{(2)}(\boldsymbol{k}) = &\left(-m + \sum_{j=x,y,z} t_j \cos k_j\right)\mu_0\tau_3 \\ &+ v_x \sin k_x \mu_0\tau_1\sigma_3 + v_y \sin k_y \mu_3\tau_1\sigma_1 \\ &+ v_z \sin k_z \mu_0\tau_1\sigma_2 \\ &+ (v_{ab1} + v_{ab2}\cos k_x)\sin\frac{k_z}{2}\mu_1\tau_1\sigma_1. \end{aligned} \tag{4}$$

Both $\mathcal{H}_{\mathrm{TCI}}^{(1)}(\boldsymbol{k})$ and $\mathcal{H}_{\mathrm{TCI}}^{(2)}(\boldsymbol{k})$ have the same TCI phase, and the similar dependence of the surface states on the surface orientations (see Supplemental Material No. 5 [51]).

We calculate the surface energies $E_{\mathrm{surf}}^{(010)}$ and $E_{\mathrm{surf}}^{(\alpha 0\gamma)}$ of this model for various surface orientations up to maximum absolute values of the Miller index $(\alpha_{\max}, \gamma_{\max}) = (3, 9)$, where $E_{\mathrm{surf}}^{(\alpha\beta\gamma)}$ is defined by Eq. (S.3) in the Supplemental Material No. 1 [51]. According to the Wulff construction [11], we can obtain the equilibrium crystal shape minimizing the total surface energy as the following 3D region:

$$\mathcal{W} = \bigcap_{\boldsymbol{n}_{\alpha\beta\gamma}\in S^2} \Gamma_{\boldsymbol{n}_{\alpha\beta\gamma}}, \tag{5}$$

$$\Gamma_{\boldsymbol{n}_{\alpha\beta\gamma}} = \{\boldsymbol{r}\in\mathbb{R}^3 | \boldsymbol{r}\cdot\boldsymbol{n}_{\alpha\beta\gamma} \le E_{\mathrm{surf}}^{(\alpha\beta\gamma)}\}, \tag{6}$$

where $\boldsymbol{n}_{\alpha\beta\gamma}$ is the outward unit normal vector to the $(\alpha\beta\gamma)$ surface, and S^2 is the unit sphere. By using the WULFFPACK package [62], we obtain this shape from $E_{\mathrm{surf}}^{(\alpha\beta\gamma)}$. Figures 2(a-1) and 2(b-1) show the equilibrium crystal shapes of $\mathcal{H}_{\mathrm{TCI}}^{(2)}(\boldsymbol{k})$ with the trivial insulator phase and the TCI phase, respectively. We show the dependence of the surface energies on the surface orientations as a function of the angle θ between the surface and the (100) plane, defined by $\tan\theta = \gamma/\alpha$ [Figs. 2(a-2) and 2(b-2)]. To analyze the results, we introduce the following trial function:

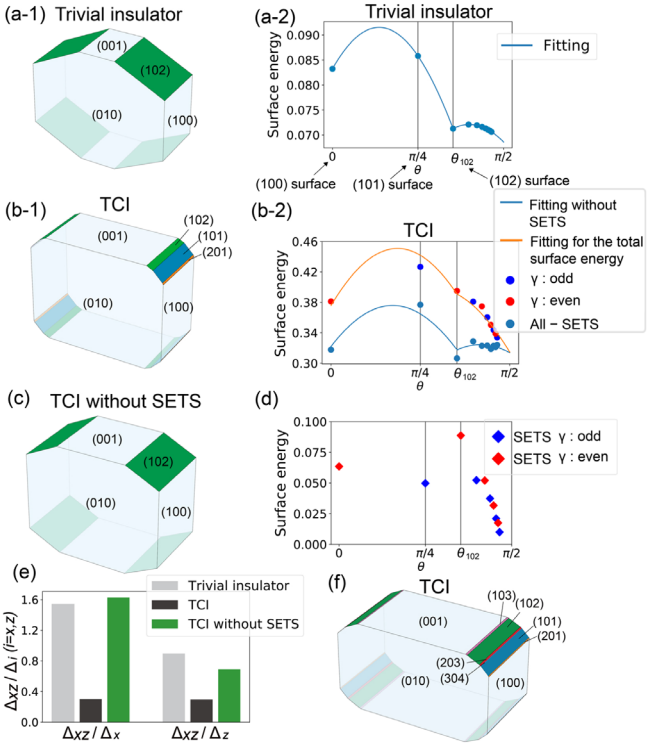

FIG. 2. (a), (b) Equilibrium crystal shapes and surface energies of $\mathcal{H}_{\mathrm{TCI}}^{(2)}(\boldsymbol{k})$ with the parameters $t_x = t_y = t_z = 1$, $v_{ab1} = 0.8$, and $v_{ab2} = 1.2$. The other parameters are $m = 6$, $v_x = v_z = 0.4$, and $v_y = 0.6$ in (a) and $m = 2$, $v_x = v_y = v_z = 0.4$ in (b). The (10γ) surface energy from $\gamma = 0$ to $\gamma = 9$. The dots are determined by $E_{\mathrm{surf}}^{(\alpha\beta\gamma)}$. (a-2) The surface energy can be fitted with $F(\theta)$ with $\Delta_x = 0.02218$, $\Delta_z = 0.03806$, and $\Delta_{xz} = 0.03414$. (b-2) We fit the total surface energy (orange) and the total surface energy without the SETS (blue) with $F(\theta)$ with $\Delta_x = 0.2445$, $\Delta_z = 0.2490$, and $\Delta_{xz} = 0.07343$ in the former case and $\Delta_x = 0.08238$, $\Delta_z = 0.1940$, and $\Delta_{xz} = 0.1340$ in the latter case. (c) The equilibrium crystal shape from the surface energies of (b-2) without the SETS. (d) The SETS in the TCI. (e) Comparison of Δ_{xz}/Δ_i $(i = x, z)$ for the trivial insulator in (a-2), the TCI [orange fitting in (b-2)], and the TCI without the SETS [blue fitting in (b-2)]. (f) The equilibrium crystal shape when $\mathcal{H}_{\mathrm{TCI}}^{(2)}(\boldsymbol{k})$ has the more distant hopping term with $m = 2$, $t_x = t_y = t_z = 1$, $v_x = 0.4$, $v_y = 0.6$, $v_z = 0.2$, $v_{ab1} = 0.8$, $v_{ab2} = 0.9$, and $v_{ab3} = 0.8$.

$$\begin{aligned}F(\theta) = &\Delta_x\cos|\theta| + \Delta_z\sin|\theta| \\ &+ \Delta_{xz}\sin|\theta-\theta_{102}| + \Delta_{xz}\sin|\theta+\theta_{102}|, \end{aligned} \tag{7}$$

where θ_{102} is the angle satisfying $\cos\theta_{102} = 1/\sqrt{5}$ and $\sin\theta_{102} = 2/\sqrt{5}$. This function can be obtained by the analysis in terms of the numbers of dangling bonds on the surface (see Supplemental Material No. 6 [51]). The surface energy of the trivial insulator can be fitted perfectly with $F(\theta)$ [Fig. 2(a-2)], and therefore the facets of the trivial insulator are determined mainly by the surface energy from chemical bonding (SECB).

Next, we discuss the surface energy of the TCI in Fig. 2(b-2). The appearance of the (101) and the (201) facets in Fig. 2(b-1) suggests a new mechanism other than the SECB. Here, we attribute it to the surface energy obtained only from the bands forming the Dirac cones. We refer to this as the surface energy from topological surface states (SETS), which is defined by Eq. (S.4) in Supplemental Material No. 1 [51]. Figure 2(b-2) also shows the total energy minus the SETS. We fit the total surface energy and the total surface energy without the SETS with Eq. (7), and in the latter fitting a sharp dip at $\theta = \theta_{102}$ appears, which is similar to the surface energy in the trivial insulator in Fig. 2(b-1). In addition, we calculate the equilibrium crystal shape from the surface energies of the TCI without the SETS [Fig. 2(c)]. This result shows that the (101) and the (201) facets are due to the SETS. Figure 2(d) also shows the SETS in the TCI.

We confirm the above interpretation by analyzing the fitting data for Δ_x, Δ_z, and Δ_{xz}. Figure 2(e) shows a comparison of Δ_{xz}/Δ_i $(i = x, z)$ for the cases corresponding to Figs. 2(a-1), 2(b-1), and 2(c). In the trivial insulator, Δ_x, Δ_z, and Δ_{xz} are of a similar order of magnitude, corresponding to hoppings almost isotropically distributed in the xz plane. In the TCI phase, the hopping parameters used in our calculation are almost the same as the trivial insulator phase, but unexpectedly, Δ_x, Δ_z, and Δ_{xz} become quite anisotropic [Fig. 2(e)]. We see from Fig. 2(e) that it restores the isotropic behavior by subtracting the SETS. A more detailed discussion is in Supplemental Material No. 5 [51]. Thus, we conclude that the unique crystal shape of the TCI are due to the SETS. Figure 2(f) also shows the crystal shape when we add a more distant hopping term $v_{ab3}\cos 2k_x \sin(k_z/2)\mu_1\tau_1\sigma_1$ to $\mathcal{H}^{(2)}_{\mathrm{TCI}}(\boldsymbol{k})$. In this case, the additional facets appear because of the interplay between the SETS and the SECB from the bonds in various directions.

Material realization.—Here, we show that these singular surface states can be realized in KHgSb proposed as a $\hat{G}_x$-symmetric TCI with space group #194 [47], where $\hat{G}_x = \{M_x|\frac{1}{2}\hat{\boldsymbol{z}}\}$ with M_x being a mirror reflection with the yz mirror plane. It has a phase transition to #186 when $T <$ 150 K [63], and here we will discuss the low-temperature phase with #186. Figures 3(a) and 3(b) show the crystal structures of KHgSb. Figure 3(c) is the Brillouin zone and the (010) surface Brillouin zone. To make it easier to see whether the surfaces are glide-invariant or not, we double the original hexagonal unit cell and take an orthorhombic unit cell with the lattice vectors $\boldsymbol{a}_1 = (A, 0, 0)$, $\boldsymbol{a}_2 = (0, B, 0)$, and $\boldsymbol{a}_3 = (0, 0, C)$, where A, B, and C are lattice constants. The enlarged unit cell leads to a translation symmetry given by $\hat{T} = \{E|\frac{1}{2}\boldsymbol{a}_1 + \frac{1}{2}\boldsymbol{a}_2\}$. The index $(\alpha\beta\gamma)$ in this orthorhombic lattice is different from the conventional Miller index in hexagonal crystals.

Next, we consider the conditions for the $(\alpha\beta\gamma)$ surface to be glide-symmetric in these symmetry settings. Let a plane P be the $(\alpha\beta\gamma)$ plane. Under $\hat{G}_x$, the plane P is transformed into $\tilde{P}$. The plane P is glide-symmetric when $\tilde{P}$ is equivalent to either P or P', where P' is the plane transformed from P via $\hat{T}$. In the former case, the index satisfies (i) $\alpha = 0$ and $\gamma \equiv 0 \pmod 2$, and in the latter case, the index satisfies (ii) $\alpha = 0$ and $\beta - \gamma \equiv 0 \pmod 2$. When the index satisfies (i) or (ii), the $(\alpha\beta\gamma)$ surface is symmetric under the glide $\hat{G}_x$ symmetry.

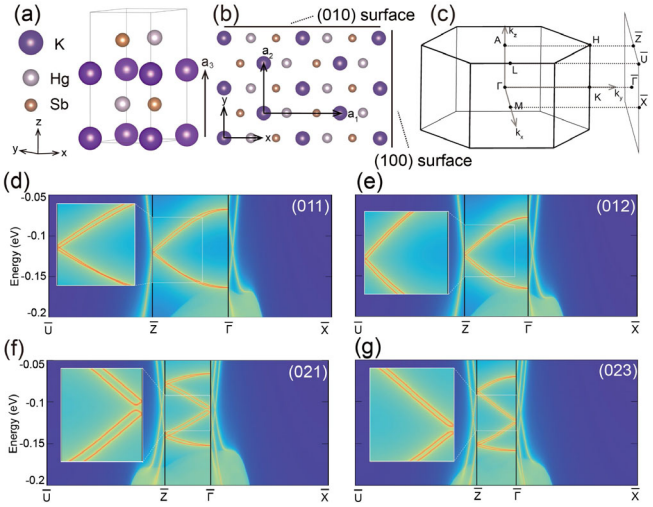

FIG. 3. (a), (b) Crystal structure of KHgSb. (c) The bulk Brillouin zone and the (010) surface Brillouin zone for KHgSb with space group #186. (d)–(g) Surface states of KHgSb for various surfaces.

The surface states on four different surfaces are shown in Figs. 3(d)–3(g), which have gapless hourglass surface states for the (011) and (012) surfaces because of the presence of the glide symmetry, but gapped surface states for the (021) and (023) surfaces because of the absence of the glide symmetry. These results are consistent with our analysis in terms of symmetries in the previous paragraph and can be observed by angle-resolved photoemission spectroscopy. Because these results are due to the glide symmetry, a similar result is expected in the high-temperature phase with space group #194. On the other hand, the gaps of the (021) and the (023) surface states are 2.4 meV and 2.6 meV, respectively. Therefore, the surface gap is smaller than temperatures in crystal growth, and the effects of these small band gaps cannot be reflected in crystal shapes in this material.

The smallness of the gaps on the glide-asymmetric surface states in KHgSb is attributed to weak interlayer coupling of KHgSb [63]. The gaps on the glide-asymmetric surfaces are proportional to the strength of the interlayer couplings, as seen from the calculation of $\mathcal{H}^{(1)}_{\mathrm{TCI}}(\boldsymbol{k})$. Thus, the glide-symmetric TCIs with stronger interlayer coupling are suitable for experiments. In addition, nanocrystals are suitable for experimental realization of equilibrium crystal shapes.

Summary and Discussion.—Here, we discuss another type of TCI, i.e., a TCI with surface states protected by a mirror M_y symmetry. The surface states can affect the equilibrium crystal shapes. On the other hand, in this Letter, we theoretically show novel dependence of presence or absence of gapless topological surface states on the parity of the surface Miller index. This is unique to the TCI protected by glide symmetry. As we show in Supplemental Material No. 8 [51], the gapless surface states survive surface reconstructions. We discovered that the topological surface states significantly affect the facets realized in the TCI by calculations of the model. The facets of the TCI can be determined by the interplay between the surface energy from chemical bonding and that from the topological surface states.

We thank Toru Hirahara, Ryo Okugawa, Kazuki Yokomizo, and Ryo Takahashi for fruitful discussions. This work was supported by Japan Society for the Promotion of Science (JSPS) KAKENHI Grants No. JP18H03678, JP18K03500, JP20H04633, JP21J22264, JP21K13865, and JP22H00108, and by Elements Strategy Initiative to Form Core Research Center (TIES), from MEXT Grant No. JPMXP0112101001.

[1] M. A. Lovette, A. R. Browning, D. W. Griffin, J. P. Sizemore, R. C. Snyder, and M. F. Doherty, Crystal shape engineering, Ind. Eng. Chem. Res. **47**, 9812 (2008).
[2] E. Auyeung, T. I. Li, A. J. Senesi, A. L. Schmucker, B. C. Pals, M. O. de La Cruz, and C. A. Mirkin, DNA-mediated nanoparticle crystallization into Wulff polyhedra, Nature (London) **505**, 73 (2014).
[3] S. Yang, B. X. Yang, L. Wu, Y. H. Li, P. Liu, H. Zhao, Y. Y. Yu, X. Q. Gong, and H. G. Yang, Titania single crystals with a curved surface, Nat. Commun. **5**, 5355 (2014).
[4] G. Liu, H. G. Yang, J. Pan, Y. Q. Yang, G. Q. Lu, and H.-M. Cheng, Titanium dioxide crystals with tailored facets, Chem. Rev. **114**, 9559 (2014).
[5] Y. Sun and Y. Xia, Shape-controlled synthesis of gold and silver nanoparticles, Science **298**, 2176 (2002).
[6] H. G. Yang, C. H. Sun, S. Z. Qiao, J. Zou, G. Liu, S. C. Smith, H. M. Cheng, and G. Q. Lu, Anatase TiO_2 single crystals with a large percentage of reactive facets, Nature (London) **453**, 638 (2008).
[7] E. Ringe, R. P. Van Duyne, and L. Marks, Wulff construction for alloy nanoparticles, Nano Lett. **11**, 3399 (2011).
[8] R. Tran, Z. Xu, B. Radhakrishnan, D. Winston, W. Sun, K. A. Persson, and S. P. Ong, Surface energies of elemental crystals, Sci. Data **3**, 160080 (2016).
[9] M. W. Anderson, J. T. Gebbie-Rayet, A. R. Hill, N. Farida, M. P. Attfield, P. Cubillas, V. A. Blatov, D. M. Proserpio, D. Akporiaye, B. Arstad, and J. D. Gale, Predicting crystal growth via a unified kinetic three-dimensional partition model, Nature (London) **544**, 456 (2017).
[10] S. Wang, G. Liu, and L. Wang, Crystal facet engineering of photoelectrodes for photoelectrochemical water splitting, Chem. Rev. **119**, 5192 (2019).
[11] G. Wulff, Zur Frage der Geschwindigkeit des Wachstums und der Auflösung der Krystallflagen, Z. Kristallogr. **34**, 449 (1901).
[12] M. von Laue, Der Wulffsche Satz für die Gleichgewichtsform von Kristallen, Z. Kristallogr. **105**, 124 (1943).
[13] C. Herring, Some theorems on the free energies of crystal surfaces, Phys. Rev. **82**, 87 (1951).
[14] L. D. Marks, Experimental studies of small particle structures, Rep. Prog. Phys. **57**, 603 (1994).
[15] G. D. Barmparis, Z. Lodziana, N. Lopez, and I. N. Remediakis, Nanoparticle shapes by using Wulff constructions and first-principles calculations, Beilstein J. Nanotechnol. **6**, 361 (2015).
[16] Y. Xia, Y. Xiong, B. Lim, and S. Skrabalak, Shape-controlled synthesis of metal nanocrystals: Simple chemistry meets complex physics?, Angew. Chem. Int. Ed. **48**, 60 (2009).
[17] W. Haiss, Surface stress of clean and adsorbate-covered solids, Rep. Prog. Phys. **64**, 591 (2001).
[18] I. Galanakis, N. Papanikolaou, and P. Dederichs, Applicability of the broken-bond rule to the surface energy of the fcc metals, Surf. Sci. **511**, 1 (2002).
[19] F. Ma and K.-W. Xu, Using dangling bond density to characterize the surface energy of nanomaterials, Surf. Interface Anal. **39**, 611 (2007).
[20] J. G. Eberhart and S. Horner, Bond-energy and surface-energy calculations in metals, J. Chem. Educ. **87**, 608 (2010).
[21] L. Fu, Topological Crystalline Insulators, Phys. Rev. Lett. **106**, 106802 (2011).
[22] T. H. Hsieh, H. Lin, J. Liu, W. Duan, A. Bansil, and L. Fu, Topological crystalline insulators in the SnTe material class, Nat. Commun. **3**, 982 (2012).
[23] K. Shiozaki and M. Sato, Topology of crystalline insulators and superconductors, Phys. Rev. B **90**, 165114 (2014).
[24] Z. Li, S. Shao, N. Li, K. McCall, J. Wang, and S. Zhang, Single crystalline nanostructures of topological crystalline insulator SnTe with distinct facets and morphologies, Nano Lett. **13**, 5443 (2013).
[25] M. Safdar, Q. Wang, M. Mirza, Z. Wang, and J. He, Crystal shape engineering of topological crystalline insulator SnTe microcrystals and nanowires with huge thermal activation energy gap, Cryst. Growth Des. **14**, 2502 (2014).
[26] B. Bradlyn, L. Elcoro, J. Cano, M. Vergniory, Z. Wang, C. Felser, M. Aroyo, and B. A. Bernevig, Topological quantum chemistry, Nature (London) **547**, 298 (2017).
[27] H. C. Po, A. Vishwanath, and H. Watanabe, Symmetry-based indicators of band topology in the 230 space groups, Nat. Commun. **8**, 50 (2017).
[28] J. Kruthoff, J. de Boer, J. van Wezel, C. L. Kane, and R.-J. Slager, Topological Classification of Crystalline Insulators through Band Structure Combinatorics, Phys. Rev. X **7**, 041069 (2017).
[29] Z. Song, T. Zhang, Z. Fang, and C. Fang, Quantitative mappings between symmetry and topology in solids, Nat. Commun. **9**, 3530 (2018).
[30] E. Khalaf, H. C. Po, A. Vishwanath, and H. Watanabe, Symmetry Indicators and Anomalous Surface States of Topological Crystalline Insulators, Phys. Rev. X **8**, 031070 (2018).

[31] F. Schindler, A. M. Cook, M. G. Vergniory, Z. Wang, S. S. Parkin, B. A. Bernevig, and T. Neupert, Higher-order topological insulators, Sci. Adv. **4**, eaat0346 (2018).

[32] Z. Song, S.-J. Huang, Y. Qi, C. Fang, and M. Hermele, Topological states from topological crystals, Sci. Adv. **5**, eaax2007 (2019).

[33] C. Fang and L. Fu, New classes of topological crystalline insulators having surface rotation anomaly, Sci. Adv. **5**, eaat2374 (2019).

[34] Y. Tanaka, R. Takahashi, and S. Murakami, Appearance of hinge states in second-order topological insulators via the cutting procedure, Phys. Rev. B **101**, 115120 (2020).

[35] R. Takahashi, Y. Tanaka, and S. Murakami, Bulk-edge and bulk-hinge correspondence in inversion-symmetric insulators, Phys. Rev. Research **2**, 013300 (2020).

[36] K. Shiozaki, M. Sato, and K. Gomi, Z_2 topology in nonsymmorphic crystalline insulators: Möbius twist in surface states, Phys. Rev. B **91**, 155120 (2015).

[37] C. Fang and L. Fu, New classes of three-dimensional topological crystalline insulators: Nonsymmorphic and magnetic, Phys. Rev. B **91**, 161105(R) (2015).

[38] L. Lu, C. Fang, L. Fu, S. G. Johnson, J. D. Joannopoulos, and M. Soljačić, Symmetry-protected topological photonic crystal in three dimensions, Nat. Phys. **12**, 337 (2016).

[39] H. Kim and S. Murakami, Emergent spinless Weyl semimetals between the topological crystalline insulator and normal insulator phases with glide symmetry, Phys. Rev. B **93**, 195138 (2016).

[40] D. Chen, T.-T. Zhang, C.-J. Yi, Z.-D. Song, W.-L. Zhang, T. Zhang, Y.-G. Shi, H.-M. Weng, Z. Fang, P. Richard, and H. Ding, Robustness of topological states with respect to lattice instability in the nonsymmorphic topological insulator KHgSb, Phys. Rev. B **96**, 064102 (2017).

[41] B. J. Wieder, B. Bradlyn, Z. Wang, J. Cano, Y. Kim, H.-S. D. Kim, A. M. Rappe, C. Kane, and B. A. Bernevig, Wallpaper fermions and the nonsymmorphic Dirac insulator, Science **361**, 246 (2018).

[42] H. Kim, K. Shiozaki, and S. Murakami, Glide-symmetric magnetic topological crystalline insulators with inversion symmetry, Phys. Rev. B **100**, 165202 (2019).

[43] H. Kim and S. Murakami, Glide-symmetric topological crystalline insulator phase in a nonprimitive lattice, Phys. Rev. B **102**, 195202 (2020).

[44] Y. Tanaka, R. Takahashi, T. Zhang, and S. Murakami, Theory of inversion-$\mathbb{Z}_4$ protected topological chiral hinge states and its applications to layered antiferromagnets, Phys. Rev. Research **2**, 043274 (2020).

[45] C.-X. Liu, R.-X. Zhang, and B. K. VanLeeuwen, Topological nonsymmorphic crystalline insulators, Phys. Rev. B **90**, 085304 (2014).

[46] K. Shiozaki, M. Sato, and K. Gomi, Topology of nonsymmorphic crystalline insulators and superconductors, Phys. Rev. B **93**, 195413 (2016).

[47] Z. Wang, A. Alexandradinata, R. J. Cava, and B. A. Bernevig, Hourglass fermions, Nature (London) **532**, 189 (2016).

[48] I. C. Fulga, N. Avraham, H. Beidenkopf, and A. Stern, Coupled-layer description of topological crystalline insulators, Phys. Rev. B **94**, 125405 (2016).

[49] H. Song, S.-J. Huang, L. Fu, and M. Hermele, Topological Phases Protected by Point Group Symmetry, Phys. Rev. X **7**, 011020 (2017).

[50] S.-J. Huang, H. Song, Y.-P. Huang, and M. Hermele, Building crystalline topological phases from lower-dimensional states, Phys. Rev. B **96**, 205106 (2017).

[51] See Supplemental Material at http://link.aps.org/supplemental/10.1103/PhysRevLett.129.046802 for further details on our effective surface theory of the TCI, the $(\alpha 0 \gamma)$ surface with $\gamma \neq 1$, 2, the tight-binding models, the TCI without $\mathcal{T}$ symmetry, the Wulff construction, the methods to calculate the surface energy $E_{\mathrm{surf}}^{(\alpha\beta\gamma)}$ and the SETS, the derivation of the function $F(\theta)$ based on the numbers of dangling bonds on the surface, and the methods of the first-principles calculations, which includes Refs. [52–60].

[52] J. P. Perdew, K. Burke, and M. Ernzerhof, Generalized Gradient Approximation Made Simple, Phys. Rev. Lett. **77**, 3865 (1996).

[53] G. Kresse and J. Furthmüller, Efficient iterative schemes for *ab initio* total-energy calculations using a plane-wave basis set, Phys. Rev. B **54**, 11169 (1996).

[54] N. Marzari and D. Vanderbilt, Maximally localized generalized Wannier functions for composite energy bands, Phys. Rev. B **56**, 12847 (1997).

[55] M. L. Sancho, J. L. Sancho, J. L. Sancho, and J. Rubio, Highly convergent schemes for the calculation of bulk and surface Green functions, J. Phys. F **15**, 851 (1985).

[56] M. L. Sancho, J. L. Sancho, and J. Rubio, Quick iterative scheme for the calculation of transfer matrices: Application to Mo (100), J. Phys. F **14**, 1205 (1984).

[57] Q. Wu, S. Zhang, H.-F. Song, M. Troyer, and A. A. Soluyanov, WannierTools: An open-source software package for novel topological materials, Comput. Phys. Commun. **224**, 405 (2018).

[58] R. Yu, X. L. Qi, A. Bernevig, Z. Fang, and X. Dai, Equivalent expression of $\mathbb{Z}_2$ topological invariant for band insulators using the non-Abelian Berry connection, Phys. Rev. B **84**, 075119 (2011).

[59] A. Alexandradinata, X. Dai, and B. A. Bernevig, Wilson-loop characterization of inversion-symmetric topological insulators, Phys. Rev. B **89**, 155114 (2014).

[60] X.-L. Qi, T. L. Hughes, and S.-C. Zhang, Topological field theory of time-reversal invariant insulators, Phys. Rev. B **78**, 195424 (2008).

[61] PythTB, http://physics.rutgers.edu/pythtb/.

[62] J. M. Rahm and P. Erhart, WulffPack: A Python package for Wulff constructions, J. Open Source Softwaare **5**, 1944 (2020).

[63] D. Chen, T.-T. Zhang, C.-J. Yi, Z.-D. Song, W.-L. Zhang, T. Zhang, Y.-G. Shi, H.-M. Weng, Z. Fang, P. Richard, and H. Ding, Robustness of topological states with respect to lattice instability in the nonsymmorphic topological insulator KHgSb, Phys. Rev. B **96**, 064102 (2017).